

# HI studies of the Sculptor group galaxies.

## VIII. The background galaxies: NGC 24 and NGC 45

Laurent Chemin<sup>1,2</sup>, Claude Carignan<sup>1</sup>, Nathalie Drouin<sup>1</sup>, and Kenneth C. Freeman<sup>3</sup>  
 [chemin,carignan]@astro.umontreal.ca, kcf@mso.anu.edu.au

### ABSTRACT

In order to complete our HI survey of galaxies in the Sculptor group area, VLA observations of NGC 24 and NGC 45 are presented. These two galaxies of similar magnitude  $M_B \sim -17.4$  lie in the background of the Sculptor group and are low surface brightness galaxies, especially NGC 45. The HI distribution and kinematics are regular for NGC 24 while NGC 45 exhibits a kinematical twist of its major axis. A tilted-ring model shows that the position angle of the major axis changes by  $\sim 25^\circ$ . A best-fit model of their mass distribution gives mass-to-light ratios for the stellar disk of 2.5 and 5.2 for NGC 24 and NGC 45 respectively. These values are higher than the ones expected from stellar population synthesis models. Despite the large dark matter contribution, the galaxy mass is still dominated by the stellar component in their very inner regions. These high mass-to-light ratios are typical of what is seen in low surface brightness galaxies and may indicate that, in those galaxies, disks are far from the maximum disk case. The halo parameters derived from the best-fit models are thus lower limits.

*Subject headings:* galaxies: halos — galaxies: fundamental parameter (mass) — galaxies: individual (NGC 24, NGC 45) — galaxies: kinematics and dynamics galaxies: structure

### 1. Introduction

At the beginning of the 90's, a series of papers was started on the HI properties of the Sculptor group galaxies (Puche & Carignan 1988; Carignan & Puche 1990a,b; Puche, Carignan & Bosma 1990; Puche & Carignan 1991; Puche, Carignan & van Gorkom 1991; Puche, Carignan & Wainscoat 1991). Since the Sculptor galaxies are all late-type spirals with very little or no bulge, they are ideal candidates for determining the basic dark halo parameters (Carignan & Freeman 1985). Their simple disk + halo structure makes it easier to iden-

tify the contribution of each component to the rotation curve. Also, since the HI distribution of late-type spirals is usually extended (Huchtmeier, Seiradakis & Materne 1980), it is possible to measure their rotation curve out to many disk scale lengths, an essential condition to tie down the halo parameters (Lake & Feinswog 1989).

As described in Puche & Carignan (1988), the Sculptor Group, the nearest group of galaxies from the Local Group, covers an area of  $\sim 20^\circ$  on the sky. In this area, besides the five main members studied so far (NGC 55, 247, 253, 300 and 7793), two more galaxies, NGC 24 and NGC 45 (Figure 1), fall in the same region and have similar sizes and degree of resolution as well as  $\sim 20$  known dwarf galaxies (Côté, Freeman & Carignan 1997; Côté, Carignan & Freeman 2000). However, when looking at the estimated distances, a mean distance of  $2.4 \pm 0.6$  Mpc is found for the main members (de Vaucouleurs 1978) but 6.8 Mpc ( $7\sigma$ ) and 5.9 Mpc ( $6\sigma$ ) for NGC 24 and NGC 45, respectively (based on a Hubble constant of 75

<sup>1</sup>Laboratoire d'Astrophysique Expérimentale (LAE), Observatoire du mont Mégantic, and Département de physique, Université de Montréal, C.P. 6128, Succ. Centre-Ville, Montréal, Qc, Canada H3C 3J7

<sup>2</sup>Observatoire de Paris, section Meudon, GEPI, CNRS-UMR 8111 & Université Paris 7, 5 Pl. Janssen, 92195, Meudon, France

<sup>3</sup>Research School of Astronomy and Astrophysics, Mount Stromlo Observatory, Weston Creek, ACT 2611, Australia

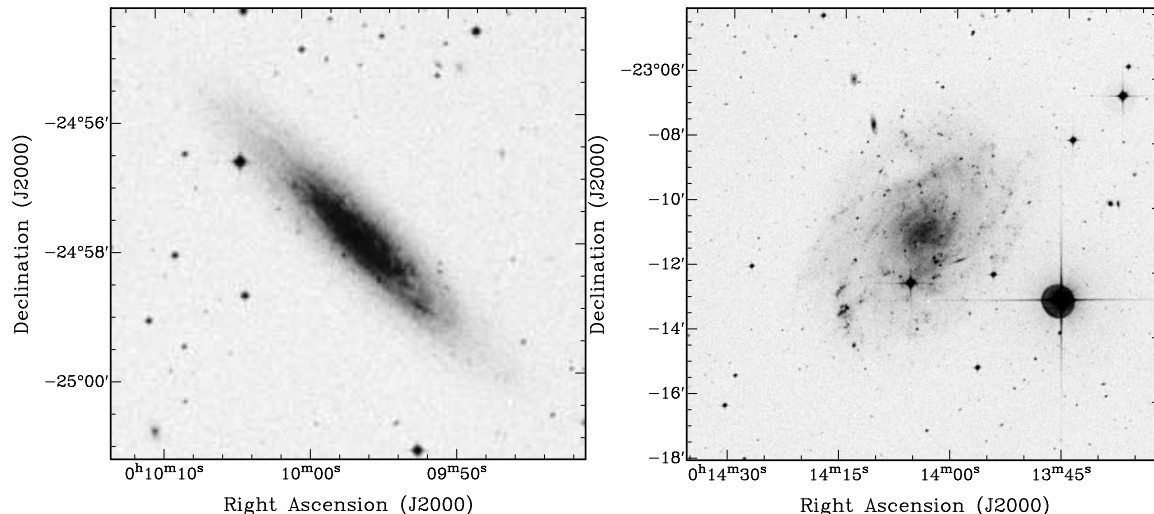


Fig. 1.— DSS blue images of NGC 24 (left) and NGC 45 (right).

$\text{km s}^{-1} \text{Mpc}^{-1}$ , Tully 1988). Moreover, when doing dynamical mass estimates of the group, any combination of the main members gives consistently  $\sim 3 \times 10^{12} M_{\odot}$  for the group, while including NGC 24 and NGC 45 makes the estimate jump to  $\sim 3 \times 10^{13} M_{\odot}$ , clearly too large for a loose group like Sculptor. All this suggests strongly that NGC 24 and NGC 45 are not members of the group but background objects.

Even if they were not members of the Sculptor group, it was decided to study them because they belong to a very interesting subgroup of galaxies called the low surface brightness (LSB) spiral galaxies, especially NGC 45. The kinematical study of LSB galaxies currently feeds the “cuspcore controversy”, (e.g. Swaters et al. 2003; Hayashi et al. 2004; de Blok 2005, and references therein). One of the many important questions which is brought to the forefront from the numerous studies of this type of object and which motivates part of the present work, is whether or not LSBs (and more generally low mass late-type spirals) can possibly form a distinct class in the Hubble sequence. The hypothesis emanating from studies on LSBs is: morphologically they belong to the spiral class, but dynamically they look more like the dwarf irregular class since they are dominated at all radii by their dark halo (Jobin & Carignan 1990; Côté, Carignan & Sancisi 1991; Martimbeau, Carignan & Roy 1994).

Moreover, a study of optical rotation curves of spiral galaxies (Buchhorn 1992) showed convincingly that the optical rotation curves in the inner parts of these galaxies give  $(M/L_B)_*$  ratios which are very high. The most likely explanation for this effect is that the dark matter component contributes a large fraction of the gravitational field even in the inner regions of LSBs galaxies (de Blok & Bosma 2002). Verheijen (1999) and Verheijen & Tully (1999) have shown convincingly the clear dichotomy between the rotation curves of HSB (high surface brightness) galaxies, which are most of the time close to the maximum disk situation, and those of LSB galaxies which are dominated at all radii by the dark matter component. Thus, in terms of their mass distribution, LSBs appear to be more closely related to dwarf irregular galaxies (e.g. DDO 154: Carignan & Freeman 1988; Carignan & Beaulieu 1989) where the luminous component is known to make a negligible contribution to the gravitational field everywhere in the disk, than to massive spirals (e.g. NGC 6946: Carignan et al 1990) where the luminous disk is the main contributor in the inner regions and the dark component only contributes significantly in the outer parts.

In order to get a better understanding of the mass distribution in NGC 24 and NGC 45, both optical and 21 cm radio observations were obtained and are presented in Section 2. In Section 3,

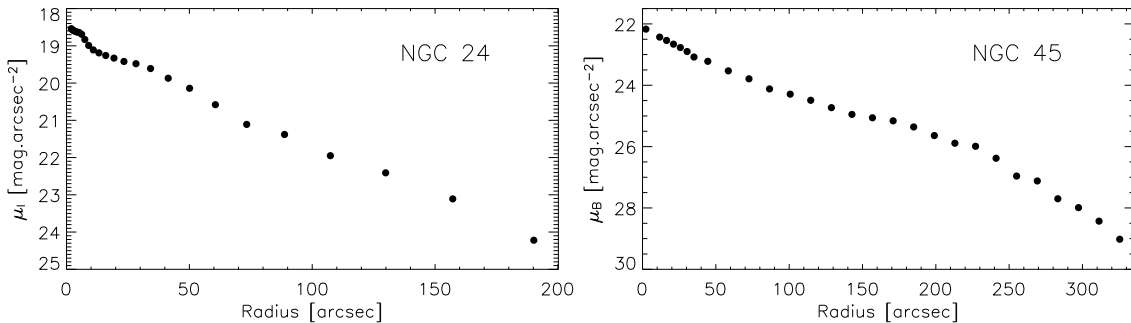


Fig. 2.—  $I$ -band luminosity profiles of NGC 24 (left) and  $B$ -band luminosity profile (Romanishin et al. 1983) of NGC 45 (right).

the luminosity profiles and the optical properties are discussed. After studying the HI content and its distribution in Section 4, Section 5 concentrates on the velocity field of these systems and presents their rotation curves. In Section 6 the data are analyzed in terms of a two component model: a luminous (stellar+gaseous) disk and a dark halo represented by an isothermal sphere potential. Finally, the discussion in Sec. 7 is followed by a summary of the results in Sec. 8.

## 2. Observations

### 2.1. Optical data

The surface photometry of NGC 24 was obtained from a set of observations in the  $I$ -band using a  $1024 \times 1024$  Thompson CCD, with the f/1 focal reducer at the prime focus of the AAT 3.9 m. The  $19 \mu\text{m}$  pixels resulted in a resolution of  $0.98''/\text{pixel}$  for a total field of  $16.7' \times 16.7'$ . The adopted mean extinction was 0.085 per airmass in the  $I$ -band. The data were obtained in 1990 September, with integration times of 20 s and 5 s. After the images were bias subtracted and flat-fielded using dark sky flats, the foreground overexposed stars were removed. Pixels within a circular region were deleted and replaced by a two dimensional surface function evaluated from the pixels lying in a surrounding background annulus. Afterwards, the sky previously evaluated by averaging the signal of many regions depleted of stars was subtracted from the galaxy image.

### 2.2. Radio data

In order to get the kinematical information needed, high sensitivity low resolution HI line observations were obtained with the Very Large Array (VLA<sup>4</sup>). They consist of 6 h observations for each galaxy (5 h on source, 1 h on calibrators), made in 1992 June. In order to get a better  $uv$  plane coverage, the hybrid DnC configuration, with larger antenna spacings in the North Arm was selected, since NGC 24 ( $\delta \simeq -25^\circ$ ) and NGC 45 ( $\delta \simeq -23^\circ$ ) are at low declinations. The candidates have been observed with a total bandwidth of 1.56 MHz divided in 128 channels and using on-line Hanning smoothing. This gives a channel separation of 12.2 kHz, corresponding to  $2.5 \text{ km s}^{-1}$ . The parameters of the synthesis observations can be found in Tables 1 and 2. No attempt to correct for the beam-smearing effect is done in this article.

First, the  $uv$  datasets were carefully examined to detect and reject bad points due to interference or crosstalk between antennae. Antennae which were shadowed by another antenna during the observations were flagged bad for the shadowing period. The data were then calibrated using the standard VLA calibration procedure. The flux scale was obtained using the continuum source 0134+329. A bandpass calibration was also applied. The reduction was done using the NRAO software package AIPS at the VLA and at the Université de Montréal.

First, by creating and inspecting a preliminary

<sup>4</sup>The NRAO is a facility of the National Science Foundation operated under cooperative agreement by Associated Universities, Inc

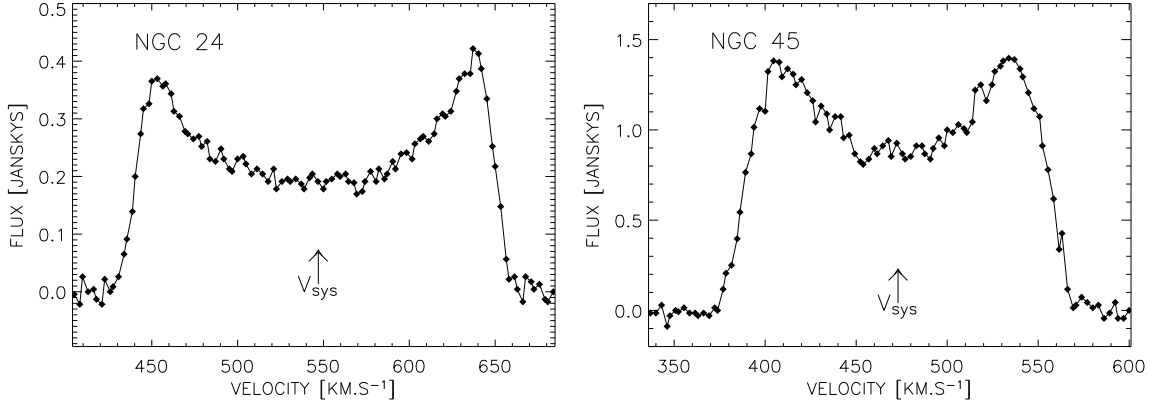


Fig. 3.— HI global profile for NGC 24 (left) and NGC 45 (right) obtained by integrating the HI emission in each channel map. The arrows indicate the systemic velocity as computed from the profiles.

series of channel maps, the channels containing only continuum radiation were identified. Next, those channels, free of emission line, were averaged in the  $uv$  plane, to represent the continuum radiation, and subtracted from all the channels. Finally, the channel maps were produced and cleaned simultaneously via a Fourier transform with natural weighting and no taper. The pixel size was  $10''$  for both systems and the original beam were convolved by circular beams of  $40'' \times 40''$  for NGC 24 and  $42'' \times 42''$  for NGC 45. This was done to make sure that all the structures that are observed are not due to the original slightly elongated beam shape. The resulting maps had a rms noise of 2.4 mJy/beam and 1.6 mJy/beam for NGC 24 and NGC 45 respectively.

### 3. Optical properties

#### 3.1. NGC 24

A study of the  $I$ -band isophotes shows that the intrinsic axis ratio varies from 0.5 near the center to 0.26 at the last measured isophote. The mean photometric parameters computed within the radius range  $1.5' - 3.0'$  are  $i = 78 \pm 5^\circ$  ( $b/a = 0.26$ ) and  $PA = 225 \pm 5^\circ$ .

The elliptically averaged luminosity profile in the  $I$ -band, illustrated in Figure 2 and listed in Table 3, was obtained using the *ellipse* task in IRAF<sup>5</sup>. In the very inner parts ( $R \leq 50''$ ) the

profile shows a decrease, probably due to internal absorption, while in the outer parts, it reveals a typical exponential decline. An exponential fit to the  $I$ -luminosity profile ( $80'' \leq R \leq 180''$ ) yields an extrapolated central surface brightness of  $19.12 \text{ mag arcsec}^{-2}$  which, when corrected for  $I$ -Galactic extinction and inclination, gives  $I(0)_c = 20.67 \text{ mag arcsec}^{-2}$ . A galactic extinction  $A_I = A_B/2.5 = 0.024$  (Draine 1989) was used, where  $A_B = 0.06$  according to de Vaucouleurs et al (1991) (hereafter referred to as RC3). The derived exponential scale length is  $\alpha^{-1} \sim 43''$ , which corresponds to  $\sim 1.42 \text{ kpc}$  at 6.8 Mpc.

When transformed to the  $B$ -band ( $\mu_B = \mu_I + 1.452$  for the Sc morphological type, from Carignan 1983<sup>6</sup>), this finally gives  $B_c(0) = 22.12 \pm 0.3 \text{ mag arcsec}^{-2}$ , which is faint relative to the Freeman canonical value of  $21.65 \pm 0.30$  for normal spiral galaxies (Freeman 1970). The central surface brightness of NGC 24 lies in the range of  $22.07 < B_c(0) < 23.70 \text{ mag}$ , as defined by Romanishin, Strom & Strom (1983) for their LSB sample, but is at the limit (within the errors) between low surface brightness objects and normal galaxies. One notices here that contrary to NGC 45, which is a genuine LSB (Romanishin et al. 1983, see §3.2) with anemic spiral arms and no

<sup>5</sup>Inc. under cooperative agreement with the NSF.

<sup>6</sup>This was derived using mean Spectral Energy Distributions (Coleman et al. 1980) for the different morphological types, convolved with the  $UBVRI$  filter responses (Bessell 1979).

<sup>5</sup>IRAF is distributed by NOAO, which is operated by AU,

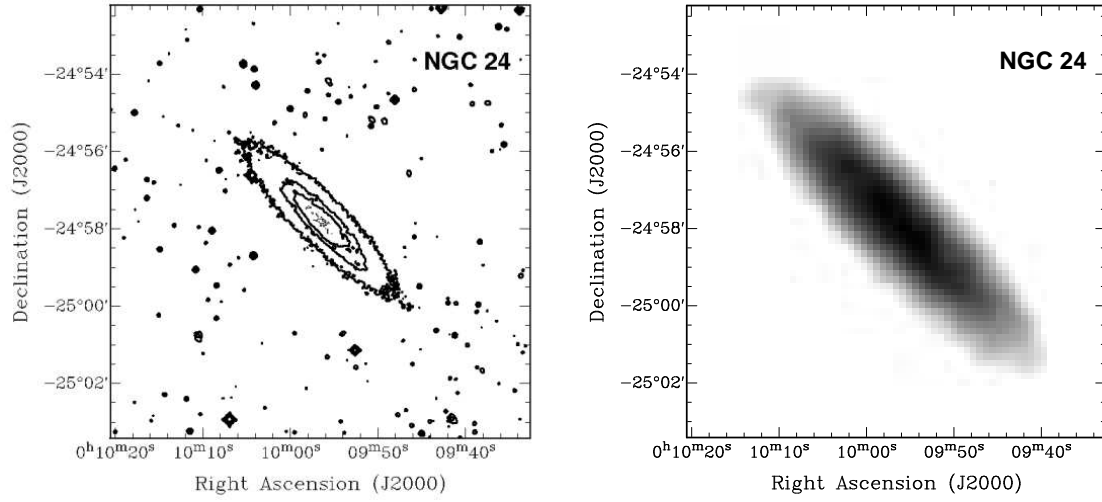


Fig. 4.— NGC 24 : Contours of the DSS optical image (left). Greyscale total HI map displayed using a logarithmic stretch (right).

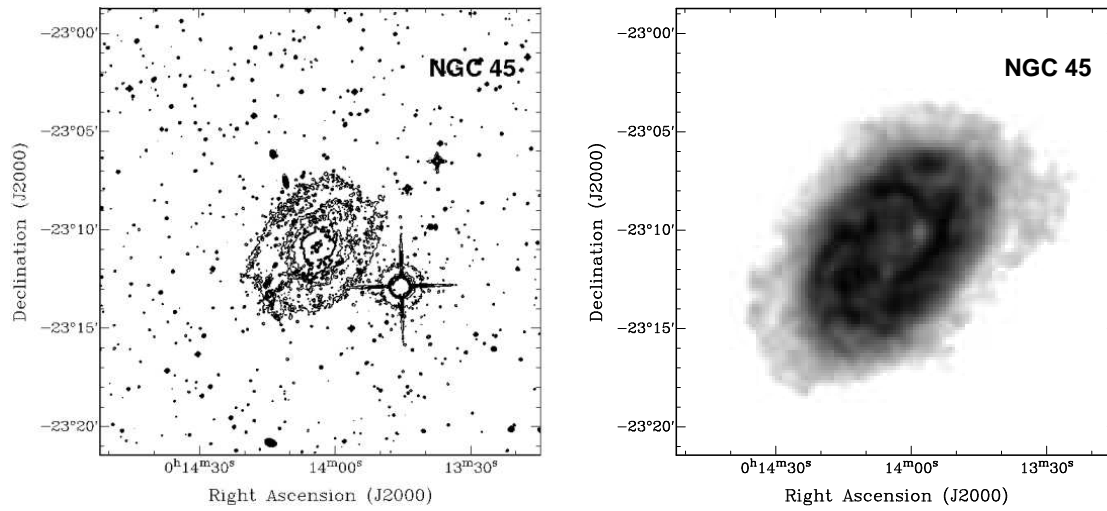


Fig. 5.— NGC 45 : Contours of the DSS optical image (left). Greyscale total HI map displayed using a logarithmic stretch (right).

evident bulge (Fig. 1), the morphological properties of NGC 24 (presence of distinct spiral arms and a small bulge) are comparable with those of high surface brightness late-type spirals.

Integrating the  $B$ -luminosity profile gives a total apparent magnitude  $B_T = 12.13$ , which is in good agreement with the value of 12.10 given by Sandage & Tammann (1987) and the value of 12.19 in RC3. When corrected for internal absorption ( $A_i/2.5 = 0.38$  (Draine 1989) where  $A_i = 0.95$  from RC3), it gives  $B_T^{0,i} = 11.75$ . At the distance of 6.8 Mpc, the corrected absolute magnitude is  $M_T^{0,i}(B) = -17.41$ . The corrected absolute magnitude corresponds to a total blue luminosity of  $1.4 \times 10^9 L_{B\odot}$ . Table 5 summarizes the optical parameters of NGC 24.

### 3.2. NGC 45

The photometric inclination is  $55 \pm 5^\circ$  and the position angle of the major axis is  $145 \pm 5^\circ$  (Puche & Carignan 1988).

A  $B$ -band surface brightness profile is used for NGC 45, as derived in Romanishin et al. (1983). We refer the reader to this article for the observational information on these data. The  $B$ -band profile is shown in Figure 2 and listed in Table 4. Romanishin et al. (1983) give an extrapolated central surface brightness  $B_c(0) = 22.51 \pm 0.46$  mag arcsec $^{-2}$  and a scale length of  $\sim 77''$ . This value translates into 2.20 kpc at our adopted distance of 5.9 Mpc. Integration of the  $B$ -band profile gives a total apparent magnitude of  $B_T = 11.48$ , which is comparable with the value of 11.10 given by Sandage & Tammann (1987) or the RC3 value of 11.32. This corresponds to an absolute magnitude  $M_T^{0,i}(B) = -17.45$  and a total blue luminosity of  $1.5 \times 10^9 L_{B\odot}$ , at the distance of 5.9 Mpc. The optical parameters are summarized in Table 6.

## 4. HI content and distribution

### 4.1. NGC 24

#### 4.1.1. Global Properties

Once the correction for the primary beam attenuation had been applied, the flux in each individual channel was summed to give the global HI profile of Figure 3 (left panel). An intensity-weighted systemic velocity of  $547 \pm 3$  km s $^{-1}$  and a midpoint heliocentric radial velocity of  $V_\odot =$

$549 \pm 3$  km s $^{-1}$  were derived. The measured profile widths at 20% and 50% levels are  $W_{20} = 218$  km s $^{-1}$  and  $W_{50} = 208$  km s $^{-1}$ . This can be compared with the HIPASS (Koribalski et al. 2004) values of  $V_\odot = 554$  km s $^{-1}$ ,  $W_{20} = 223$  km s $^{-1}$  and  $W_{50} = 210$  km s $^{-1}$ .

The integrated flux of  $54 \pm 5$  Jy km s $^{-1}$  is comparable with the HIPASS measurement of 50.3 Jy km s $^{-1}$  (Koribalski et al. 2004). It implies a total HI mass of  $(5.87 \pm 0.5) \times 10^8 \mathcal{M}_\odot$ , somewhat higher than the value of  $(4.98 \pm 0.4) \times 10^8 \mathcal{M}_\odot$  given by Huchtmeier & Seiradakis (1985) for a distance of 6.8 Mpc. It appears that no flux was missed by our synthesis observations.

#### 4.1.2. Spatial Distribution

A moment analysis (with the *momnt* task in AIPS) produced the total HI emission map of Figs. 4 (right panel, in greyscale) and 6 (left panel, expressed as column densities contours and superimposed on a DSS image of the galaxy). The distribution, which is really symmetrically distributed, stretches out to  $\sim 10'$  in diameter ( $\sim 1.3 R_{H\alpha}$  at a level of  $\sim 10^{20}$  atoms cm $^{-2}$ ). Concentric elliptical averaging corrected by a factor  $\cos i$  gave the HI radial profile illustrated in Figure 8 (left panel).

The HI surface density peaks at the center of the galaxy and then decreases as a function of radius. As compared with other morphological types of galaxies (see Fig. 10 in Swaters et al. 2002), this profile is more typical of Sd spirals (in shape and amplitude) than LSBs. Both the morphological, optical and HI properties of NGC 24 point out that this spiral can be considered at the transition between normal and LSB galaxies. This distribution will be used in Sec. 6 to derive the dynamical contribution of the HI disk.

### 4.2. NGC 45

#### 4.2.1. Global Properties

The HI properties of NGC 45 were derived in a similar way as for NGC 24. Figure 3 (right panel) gives the global HI profile once the correction for the primary beam attenuation was applied. The total flux density of  $186 \pm 19$  Jy km s $^{-1}$  (to be compared with 195.8 Jy km s $^{-1}$  in HIPASS; Koribalski et al. 2004) corresponds to an HI mass of  $(1.52 \pm 0.2) \times 10^9 \mathcal{M}_\odot$ , which is to be compared with  $(1.98 \pm 0.1) \times 10^9 \mathcal{M}_\odot$  (Huchtmeier &

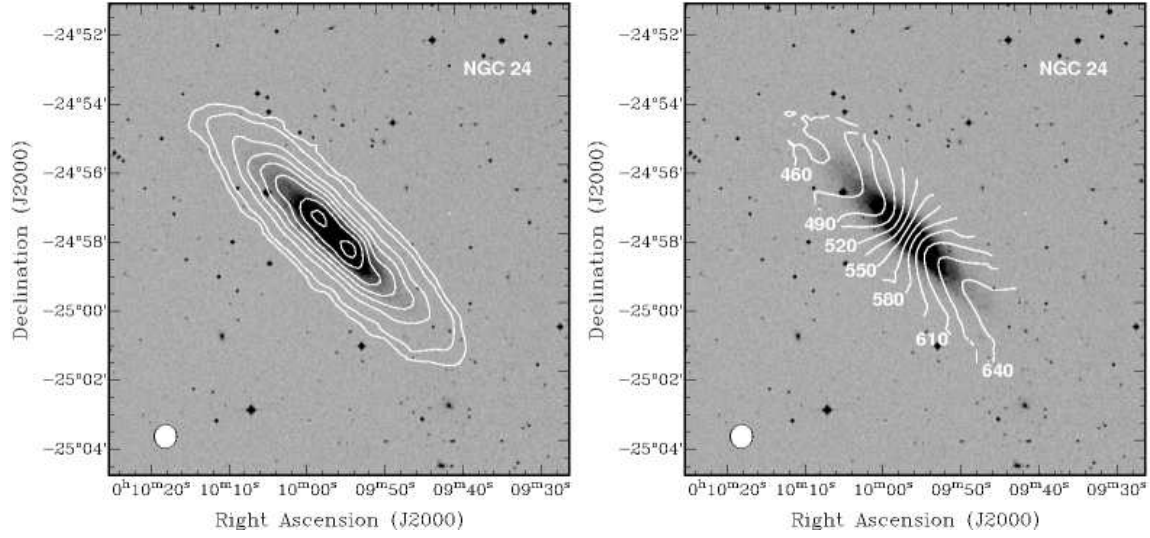


Fig. 6.— NGC 24 : Total HI map (left) and HI velocity field (right) superimposed on a DSS image of the galaxy. The contours are at surface density levels of 0.06, 0.31, 1.25, 2.19, 3.13, 4.07, 5.01 and  $5.95 \times 10^{21}$  atoms  $\text{cm}^{-2}$ . Velocity contours are drawn from 460 to 640  $\text{km s}^{-1}$  in steps of 15  $\text{km s}^{-1}$ . The beam size of  $40'' \times 40''$  is shown in the bottom left corner of the images.

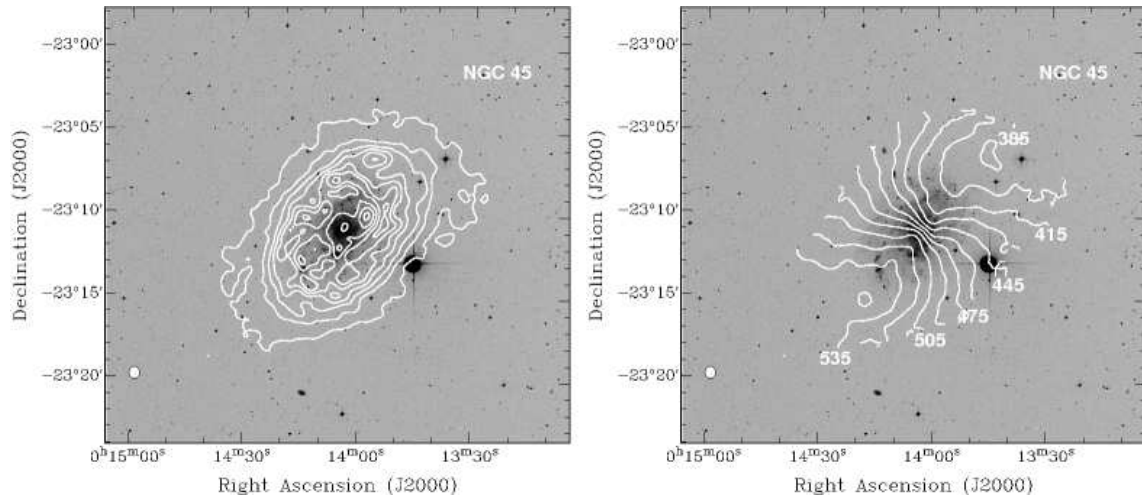


Fig. 7.— NGC 45 : Total HI map (left) and HI velocity field (right) superimposed on a DSS image of the galaxy. The contours are at surface density levels of 0.13, 0.62, 1.11, 1.60, 2.09, 2.58 and  $3.07 \times 10^{21}$  atoms  $\text{cm}^{-2}$ . Velocity contours are drawn from 385 to 550  $\text{km s}^{-1}$  in steps of 15  $\text{km s}^{-1}$ . The beam size of  $42'' \times 42''$  is shown in the bottom left corner of the images.

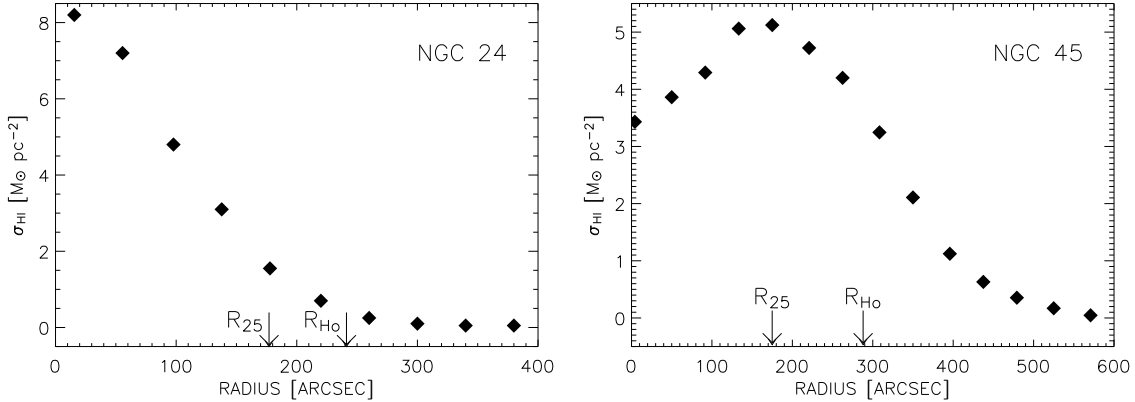


Fig. 8.— Radial distribution of HI surface density for NGC 24 (left) and NGC 45 (right), obtained by averaging the total HI map in circular annuli in the plane of the galaxy.

Seiradakis 1985) for a distance of 5.9 Mpc. This seems to indicate that  $\sim 20\%$  of the flux is missing, probably due to missing short spacings in the VLA observations. Also derived from the profile is the midpoint systemic velocity of  $470 \pm 3 \text{ km s}^{-1}$  and the intensity-weighted systemic velocity of  $473 \pm 3 \text{ km s}^{-1}$ . The measured profile widths are  $W_{20} = 180 \text{ km s}^{-1}$  and  $W_{50} = 167 \text{ km s}^{-1}$ . This can be compared to the HIPASS values of  $V_{\odot} = 467 \text{ km s}^{-1}$ ,  $W_{20} = 185 \text{ km s}^{-1}$  and  $W_{50} = 167 \text{ km s}^{-1}$  (Koribalski et al. 2004).

#### 4.2.2. Spatial Distribution

Figures 5 (right panel, in greyscale) and 7 (left panel, in contours superimposed on a DSS photograph of the galaxy) show the distribution of HI surface densities obtained by the moment analysis. The HI disk is regular and extends to  $\sim 20'$  in diameter ( $\sim 2.1 R_{\text{Ho}}$  at a level of  $\sim 10^{20} \text{ atoms cm}^{-2}$ ).

The shape and amplitude of the radial distribution of the HI surface density (Fig. 8, right panel) is typical of what is seen in low surface brightness spirals, showing a depression in the central regions with a low gas surface density level (see Fig. 10 in Swaters et al. 2002 for comparison). Both morphological, photometric and gaseous properties of NGC 45 make this spiral a genuine low surface brightness galaxy. This profile will be used in Sec. 6 to evaluate the dynamical importance of the NGC 45 HI component.

## 5. Velocity field and rotation curve

### 5.1. NGC 24

Figure 6 (right panel) shows the velocity field obtained by the moment analysis where the radial velocities were calculated by taking the intensity weighted mean of each line profile for pixels above the  $1.8\sigma$  level, in the  $40'' \times 40''$  resolution data cube. This velocity field is regular, with no sign of large-scale deviation from axial symmetry. From the shape of the isovelocity contours, one can already infer that this galaxy does not have a solid-body rotation curve (the contours are not parallel) but rather tends to be flat in the outer parts.

In order to extract the rotation curve (RC), the *rotcur* task (Begeman 1989) of the GIPSY program (van der Hulst et al. 1992) was used. The task makes a least-square fitting of a tilted-ring model to the velocity field. A solution has to be found for the following five kinematical parameters: the coordinates of the rotation center, the systemic velocity ( $v_{\text{sys}}$ ), the inclination ( $i$ ) and the position angle ( $P.A.$ ) of the major axis in order to obtain the circular velocity as a function of radius. To diminish the importance of deprojection errors at such an inclination, radial velocities in an opening angle of  $80^\circ$  about the minor axis were rejected for the least-square fitting and a cosine weighting function giving more importance to points near the major axis was used.

The fitting procedure is described in Chemin



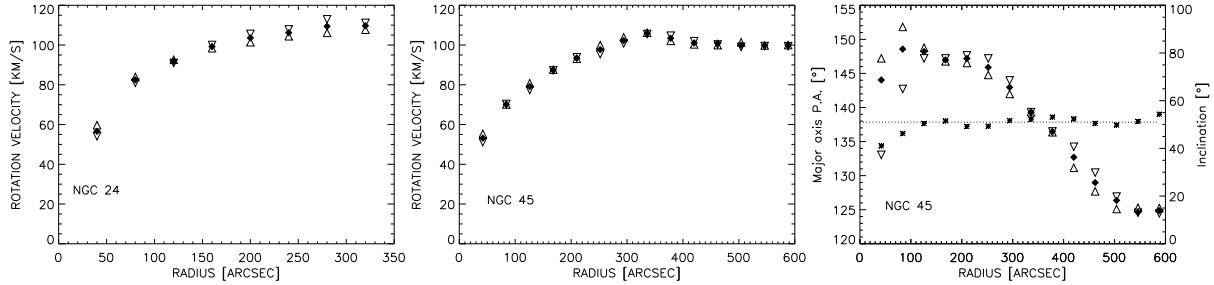


Fig. 9.— Rotation curves of NGC 24 and NGC 45 (left and central panels resp.) and radial profile of the inclination and the major axis position angle of NGC 45 (right panel), as derived from the tilted-ring models. Filled diamonds correspond to the values for both sides fitted simultaneously, open upward and downward triangles to the values for the receding and approaching sides (respectively) fitted separately. The inclination is shown as star symbols and the adopted one as a dashed line.

et al. (2006). Briefly, the rotation center and systemic velocity are first searched for, then the inclination and the position angle. The derived systemic velocity is  $554 \pm 1 \text{ km s}^{-1}$ , which is comparable to the value obtained with the global HI profile. The kinematical inclination is  $64 \pm 3^\circ$ . This is significantly lower than the optical inclination of  $78^\circ$  and the value found by an ellipse fitting to the HI isophotes ( $76^\circ$ ). The low spatial resolution of the data combined with the high inclination of the disk probably explains such a difference. The choice of either the photometric or the kinematical value does not influence the main result of this work (see Sections 6 and 7). Hence, the kinematical inclination is chosen for NGC 24 throughout the article and all derived quantities (rotation curve, mass-to-light ratio, ...) are given adopting this value, except where explicitly mentioned. The kinematical position angle is  $229 \pm 1^\circ$ . This value remains comparable with the one derived from the photometry ( $225 \pm 5^\circ$ ).

A rotation curve is finally obtained (Figure 9 and Table 7) by fixing all the other parameters at constant values because no warp is found in NGC 24. At each radius, the quoted error-bar of the velocity point given in Table 7 corresponds to the maximum value between the formal error calculated by *rotcur* ( $1\sigma$  dispersion of the fitted velocity parameter) and the largest velocity difference between the solution for both sides and the separate solutions for the approaching and receding halves (Carignan & Puche 1990a).

## 5.2. NGC 45

The velocity field of NGC 45, obtained from the analysis of the  $42'' \times 42''$  resolution data cube by discarding pixels under a  $1.6\sigma$  level, is shown in Figure 7 (right panel).

The same procedure as for NGC 24 is used to derive the RC of NGC 45. To lessen the errors due to the deprojection, all points in a sector of  $60^\circ$  around the minor axis were discarded from the fitting. A systemic velocity of  $467 \pm 2 \text{ km s}^{-1}$  is found, which agrees within the errors with the value obtained using the global profile and with the one given by Adler & Liszt (1989). The inclination is found to be constant as a function of radius ( $51 \pm 2^\circ$ ), and is in relative agreement with the photometric value within the error ( $55 \pm 5^\circ$ ).

A study of the HI isophotes shows that the outermost contour is slightly twisted with respect to the inner isophotes. The outer isovelocity contours are also twisted as a function of radius. A kinematical twist of the HI plane is indeed detected with the tilted-ring model (Figure 9). The *P.A.* decreases by  $\sim 25^\circ$  from the inner to the outer regions whereas *i* remains constant. A kinematical warp or a simple twist of the kinematical major axis is very common in the Sculptor group HI disks (e.g. Carignan & Puche 1990a), and more generally in spiral galaxies (García-Ruiz, Sancisi & Kuijken 2002).

The final rotation curve is thus derived by fixing the center coordinates, systemic velocity and inclination at constant values and by leaving the position angle free as a function of radius. The

RC is given in Table 8 and displayed in Figure 9. Here again, no significant asymmetry is detected between the RCs of the approaching and receding sides of the disk.

Table 8 also gives the radial variation of the  $P.A.$  with its errors computed as the maximum value between the formal error calculated by *rotcur* ( $1\sigma$  dispersion of the fitted angle) and the largest angle difference between the fitted value for both sides and the separate fitted values for the approaching and receding halves.

## 6. Study of the mass distribution

A preliminary study of the mass distribution is presented here using the present low resolution HI data. This should give a first good estimate of the dark-to-luminous mass ratio in those two galaxies and allow us to get a good idea whether the dark matter component dominates at all radii, as seen in dwarf irregulars (e.g. Carignan & Beaulieu 1989), in some late-type spirals (e.g. Côté et al. 1991) or in other LSB galaxies (e.g. de Blok & McGaugh 1997). As for the other papers from this series, only the best-fit mass models are presented for the two galaxies. These models are very close to the maximum disk case. Notice that for NGC 45 another model that uses the mass-to-light ratio expected from stellar populations synthesis (SPS) models is presented (see Sec. 7).

### 6.1. Two Component Model

One can refer to Carignan (1985), Carignan & Freeman (1985) and the other papers in this series for a detailed discussion of the two components (dark and luminous) model. Because NGC 24 has a very small bulge and NGC 45 has no bulge, as seen in Fig. 1, no attempt to include a bulge component in the models was made. For NGC 24, the  $I$ -profile derived in Sec. 3 was used to derive the contribution of the stellar component. It was transformed into the  $B$ -band according to Carignan (1983). For NGC 45, the B-band luminosity profile of Romanishin et al. (1983) was used. The contribution of the gaseous component was derived assuming that all the gas is confined in an infinitely thin disk and using the HI radial surface densities (Fig. 8), which were multiplied by 4/3 to take into account primordial helium.

The dark halo is modeled by an isothermal

sphere which is described by two basic parameters: the core radius  $r_c$  and the one-dimensional velocity dispersion  $\sigma$ . A third quantity, the central density of the halo, is related to the two others by  $\rho_0 = 9\sigma^2/4\pi Gr_c^2$ . Essentially, the mass model depends on three parameters: the amplitude scaling of the luminous disk  $(\mathcal{M}/L_B)_*$  (the mass-to-light ratio of the stellar disk), the radial scaling  $r_c$  and the velocity scaling  $\sigma$  of the halo. To determine the combination of the three parameters which best reproduces the observed rotation curve, a best-fitting method was used, without any constraints on the parameter values. By exploring a grid of values in the three parameter space, a set  $[(\mathcal{M}/L_B)_*, r_c, \sigma]$  is found leading to the smallest  $\chi^2$  for the fit. Once an approximate minimum has been identified, the solution is refined by improving the step resolution for the three parameters. This routine is reiterated until a final set of parameters is obtained. The mass-to-light ratio of the stellar disk is supposed to be constant as a function of radius and the errors on the derived model parameters are established from the 90% confidence level for both galaxies.

Notice that no attempt to explore different functional forms for the halo was made with these HI data. A comparison between a cuspy halo, like e.g. the NFW one (Navarro, Frenk & White 1997), and a core-dominated halo, like the one presented here, indeed requires high spatial resolution data for accurately mapping the inner rising part of a rotation curve (Swaters, Madore & Trewella 2000). Such mass models will be presented elsewhere when three-dimensional optical Fabry-Perot data will become available (Chemin et al., in prep.).

### 6.2. Mass modeling results

The results from the best-fit mass model for NGC 24 are illustrated in Figure 10 (left panel) and given in Table 9. The model gives a  $(\mathcal{M}/L_B)_*$  of  $2.5 \pm 0.3$  for a total disk mass of  $\sim 3.4 \times 10^9 \mathcal{M}_\odot$ . The HI + He gas, with a total mass of  $\sim 7.4 \times 10^8 \mathcal{M}_\odot$ , provides only  $\sim 20\%$  of the luminous mass and is therefore not very important dynamically. The parameters for the dark halo are  $r_c = 5.6 \pm 1.5$  kpc and  $\sigma = 65.0 \pm 4.0$  km s $^{-1}$ . This gives a central density for the dark halo of  $0.022 \mathcal{M}_\odot \text{pc}^{-3}$ . Notice here that the use of a rotation curve derived by a tilted-ring model with an

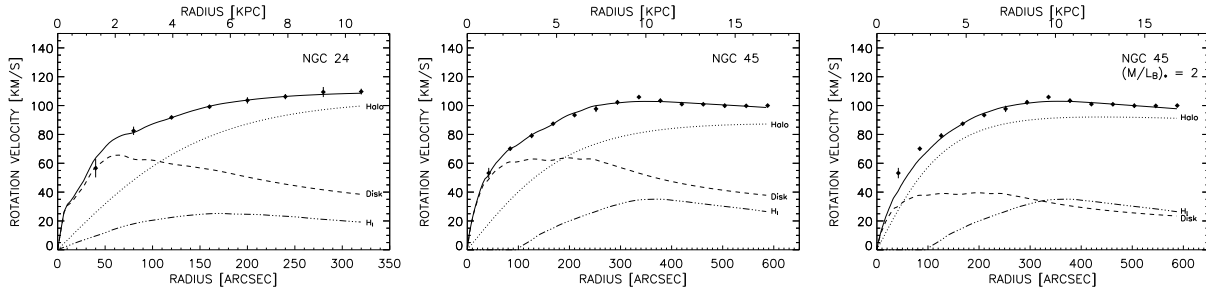


Fig. 10.— Mass models using the best-fit method for NGC 24 and NGC 45 (left and central panels resp.). The model on the right panel is for NGC 45 with  $(\mathcal{M}/L_B)_* = 2.0$ . The full line is for the best-fit model to the data (filled diamonds). The contribution of the different components (stellar disk, HI component corrected for the He content & dark halo) are identified.

inclination fixed to the photometric value of  $78^\circ$  would slightly reduce the  $(\mathcal{M}/L_B)_*$  to 2.0 without changing the other parameters.

The results from the best-fit mass model for NGC 45 are illustrated in Figure 10 (middle panel) and given in Table 10. The parameters are  $(\mathcal{M}/L_B)_* = 5.2 \pm 1.0$ ,  $r_c = 6.2 \pm 0.6$  kpc and  $\sigma = 55.0 \pm 1.0$  km s $^{-1}$ , which correspond to a central density for the halo of  $\rho = 0.013 M_\odot \text{pc}^{-3}$ . Total masses of  $5.3 \times 10^9 M_\odot$  and  $2.1 \times 10^9 M_\odot$  are found for the stellar and gaseous disks respectively.

## 7. Discussion

The extent of the HI disk is  $R_{\text{HI}} = 1.3 \times R_{\text{Ho}} = 7.3 \times \alpha^{-1}$  for NGC 24 and  $R_{\text{HI}} = 2.1 \times R_{\text{Ho}} = 7.9 \times \alpha^{-1}$  for NGC 45. The HI extent of NGC 24 is very similar to the HI extent of the Sculptor late-type spiral galaxies NGC 247, NGC 300 and NGC 7793 (1.2, 1.5 and 1.4  $R_{\text{Ho}}$ , respectively). Again, this suggests that NGC 24 is very similar to normal late-type spiral galaxies, as also claimed in §4.1.2.

The best-fit mass model of NGC 24 gives a  $(\mathcal{M}/L_B)_*$  for the stellar disk of  $2.5 \pm 0.3$ . From the observed colors of  $0.56 \lesssim (B - V) \lesssim 0.60$  for NGC 24 (de Vaucouleurs et al. 1991), SPS models predict a mass-to-light ratio for the stellar disk of  $1 \lesssim (\mathcal{M}/L_B)_* \lesssim 1.2$  (Bell & de Jong 2001). The mass-to-light ratio is thus twice the one expected from SPS models. This result remains unchanged when using  $(\mathcal{M}/L_B)_* = 2.0$ , as found when using the photometric inclination instead of the kinematical value.

The case of NGC 45 is even more problematic since the derived  $(\mathcal{M}/L_B)_*$  from the best-fit model is nearly 3 times greater than the value expected from SPS models: 5.2 versus  $1.7 \lesssim (\mathcal{M}/L_B)_* \lesssim 2.2$  (Bell & de Jong 2001), based on the observed  $(B - V)$  color of  $0.71 \pm 0.03$  (de Vaucouleurs et al. 1991).

Similar high  $(\mathcal{M}/L_B)_*$  values are often found in LSBs when fitting maximum disk models (de Blok & McGaugh 1997; de Blok, McGaugh & Rubin 2001; de Blok & Bosma 2002; Swaters et al. 2003). An interpretation of these results is that the maximum disk hypothesis must not hold for LSB galaxies (de Blok et al. 2001). As a consequence, these galaxies appear to be dominated by dark matter at all radii when mass models preferentially use a mass-to-light ratio consistent with SPS models (de Blok & McGaugh 1997; de Blok et al. 2001; de Blok & Bosma 2002).

Such a model is illustrated for NGC 45 in Figure 10 (right panel), using a  $(\mathcal{M}/L_B)_*$  of 2.0. This value is chosen to be representative of the expected  $(\mathcal{M}/L_B)_*$  range given by the SPS models (see above). Indeed, it can be seen that the dark component is dominant over almost the whole stellar disk, though with the noticeable exception of the very innermost regions.

This new model nevertheless highly underestimates the first two points of the RC, thus giving a worse fit ( $\chi^2 \sim 8$ ) than the best-fit model ( $\chi^2 \sim 3$ ). The quality of the fit also decreases as one goes towards the minimum disk hypothesis ( $(\mathcal{M}/L_B)_* = 0 / \chi^2 \sim 11$ ). Such a result is in agreement with what is found for other LSBs, as

illustrated in de Blok & Bosma (2002). For several galaxies from their sample, the minimum disk hypothesis, or a model using a low  $(\mathcal{M}/L_B)_*$ , does not always provide a better fit than the maximum disk hypothesis.

One finally notices that higher  $(\mathcal{M}/L_B)_*$  values should be expected if a correction for beam-smearing was applied or if a higher angular resolution was used for the innermost velocity points of the curves. Indeed, it should give more steeply rising rotation curves in their inner parts than the ones presented here (see e.g. Swaters et al. 2000). This would worsen the discrepancy found between the low  $(\mathcal{M}/L_B)_*$  values from SPS models and the maximum disk hypothesis. Therefore, if one finally admits that the maximum disk hypothesis is ruled out for LSBs (as favored in de Blok et al. 2001), a more cuspy halo than the pseudo isothermal sphere should perhaps be used to better fit the inner velocity points of NGC 45 with a low  $(\mathcal{M}/L_B)_*$ . This claim will be tested in a forthcoming article.

## 8. Summary and conclusions

An optical and HI study of NGC 24 and NGC 45 has been presented. The main results are as follows:

(1) From the surface photometry of NGC 24 and NGC 45, it is found that while NGC 24 is on the faint side for normal galaxies, NGC 45 can be considered as a bona fide LSB galaxy. However, both galaxies have very similar absolute magnitudes  $\sim -17.4$ .

(2) The HI distribution for NGC 24 and NGC 45 extends to  $\sim 1.3$  and  $2.1 R_{\text{Ho}}$  (respectively) at a level of  $\sim 10^{20}$  atoms  $\text{cm}^{-2}$ . The HI extent of NGC 24 is very similar to the HI extent of the Sculptor late-type spiral galaxies NGC 247, NGC 300 and NGC 7793 ( $1.2$ ,  $1.5$  and  $1.4 R_{\text{Ho}}$ , respectively).

(3) The overall velocity fields of the two galaxies are very regular. NGC 45 exhibits a twist of the kinematical major axis, showing a  $\sim 25^\circ$  variation of its major axis position angle as a function of radius. However, its disk does not have a classical warp since the inclination remains constant.

(4) The rotation curves derived from the velocity fields rise slowly and flatten at a velocity of  $\sim 110 \text{ km s}^{-1}$  and  $\sim 100 \text{ km s}^{-1}$  respectively.

It extends out to  $\sim 11$  kpc for NGC 24 and to  $\sim 17$  kpc for NGC 45, which corresponds to  $\sim 7.5$  scale lengths in both cases.

The rotation curves, combined with the luminosity profiles, were used to study the mass distribution of NGC 24 and NGC 45. Using a best-fit model, the main results are :

(1)  $(\mathcal{M}/L_B)_* = 2.5$ ,  $r_c = 5.6$  kpc and  $\sigma = 65 \text{ km s}^{-1}$  for NGC 24, and  $(\mathcal{M}/L_B)_* = 5.2$ ,  $r_c = 6.2$  kpc and  $\sigma = 55 \text{ km s}^{-1}$  for NGC 45.

(2) In both galaxies, the dark halo is the main contributor to the total mass of the galaxies with a contribution of more than  $\sim 80\%$  at the last measured point. Since the best-fit models are close to the maximum disk case, this can be considered a lower limit.

(3) The  $(\mathcal{M}/L_B)_*$  of 5.2 found for NGC 45 and 2.5 for NGC 24 are high when compared with the values predicted by stellar population synthesis models for galactic disks of same colors as NGC 24 and NGC 45. This result is similar to what is seen in other LSB galaxies. When a model for NGC 45 uses a  $(\mathcal{M}/L_B)_*$  of 2.0, which value is adopted from SPS models, it allows the galaxy mass to be entirely dominated by the dark component, but it also severely underestimates the velocity of the innermost points of the rotation curve.

This article is the first from a series that aims at measuring the shape of the mass density profile for the dark component of NGC 24 and NGC 45. When higher resolution optical kinematical H $\alpha$  data obtained with Fabry-Perot interferometry become available, more accurate mass models of those galaxies will be presented.

We would like to thank the Very Large Array for allocations of telescope time and the NRAO staff for valuable assistance. We are very grateful to Sylvie Beaulieu for her help. LC acknowledges partial support from the Fonds Québécois de la Recherche sur la Nature et les Technologies and CC from the Conseil de Recherches en Sciences Naturelles et en Génie du Canada. N.D. acknowledges financial assistance from Fonds FCAR Québec. The Digitized Sky Surveys were produced at the Space Telescope Science Institute under U.S. Government grant NAG W-2166. The images of these surveys are based on photographic data obtained using the Oschin Schmidt Telescope

on Palomar Mountain and the UK Schmidt Telescope. The plates were processed into the present compressed digital form with the permission of these institutions.

## REFERENCES

- Adler, D. S., & Liszt, H. S. 1989, *ApJ*, 339, 836
- Allen, C. W. 1976, *Astrophysical Quantities* (Athlone, London)
- Begeman, K. G. 1989, *A&A*, 223, 47
- Bell, E. F., & de Jong, R. S. 2001, *ApJ*, 550, 212
- Bessell, M. 1979, *PASP*, 91, 589
- Bottinelli, L., Gouguenheim, L., Paturel, G., & de Vaucouleurs, G. 1983, *A&A*, 118, 4
- Buchhorn, M. 1992, Ph.D. thesis, Australian National University
- Carignan, C. 1983, Ph.D. thesis, Australian National University
- Carignan, C. 1985, *ApJ*, 299, 59
- Carignan, C., & Beaulieu, S. 1989, *ApJ*, 347, 760
- Carignan, C., Charbonneau, P., Boulanger, F., & Viallefond, F. 1990, *A&A*, 234, 43
- Carignan, C., & Freeman, K.C. 1985, *ApJ*, 294, 494
- Carignan, C., & Freeman, K.C. 1988, *ApJ*, 332, L33
- Carignan, C., & Puche, D. 1990a, *AJ*, 100, 394 (paper II)
- Carignan, C., & Puche, D. 1990b, *AJ*, 100, 641 (paper IV)
- Chemin, L., Balkowski, C., Cayatte, V., Carignan, C., Amram, P., Garrido, O., Hernandez, O., Marcelin, M., Adami, C., Boselli, A., & Boulesteix, J. 2006, *MNRAS*, 366, 812
- Coleman, G. D., Wu, C. C., & Weedman, D.W. 1980, *ApJSS*, 43, 393
- Côté, S., Freeman, K. C., & Carignan, C. 1997, *AJ*, 114, 1313
- Côté, S., Carignan, C., & Freeman, K. C. 2000, *AJ*, 120, 3027
- Côté, S., Carignan, C., & Sancisi, R. 1991, *AJ*, 102, 904
- de Blok, W. J. G. 2005, *ApJ*, 634, 227
- de Blok, W. J. G., & Bosma, A. 2002, *A&A*, 385, 816
- de Blok, W. J. G., & McGaugh, S. S. 1997, *MNRAS*, 290, 533
- de Blok, W. J. G., & McGaugh, S. S., & Rubin, V. C., 2001, *AJ*, 122, 2396
- de Vaucouleurs, G. 1978, *ApJ*, 224, 710
- de Vaucouleurs, G., de Vaucouleurs, A., Corwin, H.G., Buta, R.J., Paturel G., & Fouqué, P. 1991, *Third Reference Catalogue of Bright Galaxies* (Springer, New York) (RC3)
- Draine, B.T., 1989, in *Infrared Spectroscopy in Astronomy*, Proc. of the 22nd Eslab Symposium, Ed. B. H. Kaldeich, p. 93
- Freeman, K. C. 1970, *ApJ*, 160, 811
- García-Ruiz, I., Sancisi, R., & Kuijken, K., 2002, *A&A*, 394, 769
- Hayashi, E., Navarro, J. F., Power, C., Jenkins, A., Frenk, C. S., White, S. D. M., Springel, V., Stadel, J., & Quinn, T. R. 2004, *MNRAS*, 355, 794
- Huchtmeier, W.K, & Seiradakis, J.H. 1985, *A&A*, 143, 216
- Huchtmeier, W.K, Seiradakis, J.H., & Materne, J. 1980, *A&A*, 91, 341
- Jobin, M. & Carignan, C. 1990, *AJ*, 100, 648
- Koribalski, B. S., Staveley-Smith, L., Kilborn, V. A., Ryder, S.D. et al. 2004, *AJ*, 128, 16
- Lake, G., & Feinswog, L. 1989, *AJ*, 98, 166
- Martimbeau, N., Carignan, C., & Roy, J.-R. 1994, *AJ*, 107, 543
- Navarro, J. F., Frenk, C. S., White, S. D. M. 1997, *ApJ*, 490, 493

- Puche, D., & Carignan, C. 1988, AJ, 95, 1025 (paper I)
- Puche, D., & Carignan, C. 1991, ApJ, 378, 487 (paper VII)
- Puche, D., Carignan, C., & Bosma, A. 1990, AJ, 100, 1468 (paper VI)
- Puche, D., Carignan, C., & van Gorkom, J. H. 1991, AJ, 101, 456 (paper V)
- Puche, D., Carignan, C., & Wainscoat, R. J. 1991, AJ, 101, 447 (paper III)
- Romanishin, W., Strom, K.M., & Strom, S.E. 1983, ApJS, 53, 105
- Sandage, A., & Tammann, G.A. 1987, in A Revised Shapley-Ames Catalog of Bright Galaxies, 2<sup>nd</sup>, edited by the Carnegie Institution of Washington Publication
- Swaters, R. A., Madore, B. F., & Trewhella, M. 2000, ApJ, 531, L107
- Swaters, R. A., van Albada, T. S., van der Hulst, J. M., & Sancisi, R. 2002, A&A, 390, 829
- Swaters, R. A., Madore, B. F., van den Bosch, F. C. & Balcells, M. 2003, ApJ, 583, 732
- Tully, R. B. 1988, Nearby Galaxies Catalog (Cambridge, CUP)
- van der Hulst J. M., Terlouw J. P., Begeman K. G, et al., 1992, ASP Conf. Series, 25, 131
- Verheijen, M. A. W. 1999, in Galaxy Dynamics, eds D. Merritt, J. A. Sellwood and M. Valluri, ASP Conf. Ser., 182, 383
- Verheijen, M. A. W. & Tully, B. 1999, in The Low Surface Brightness Universe, IAU Coll. 171, eds J. I. Davies, C. Impey and S. Phillipps, ASP Conf. Ser., 170, 92

TABLE 1  
PARAMETERS OF THE VLA OBSERVATIONS FOR NGC 24

Date of observation .....	1992 June 14
Time on source .....	5 <sup>h</sup>
Field center (1950.0) .....	00 <sup>h</sup> 07 <sup>m</sup> 24.0 <sup>s</sup> −25°14′30.0″
Primary beam at half-power (FWHM) .....	32′
FWHM of synthesised beam .....	40″ × 40″
Total bandwidth .....	1.56 MHz
Central velocity (heliocentric) .....	550 km s <sup>−1</sup>
Central frequency .....	1417.2489 MHz
Number of channels .....	128
Channel separation .....	12.2 kHz
Velocity Resolution .....	2.5 km s <sup>−1</sup>
RMS noise in channel maps .....	2.4 mJy/beam
Conversion factor, equivalent 1 mJy/beam area (low resolution) 40″ × 40″ .....	0.38 K
Maps gridding .....	10″ × 10″ natural weighting no taper
Flux calibrator .....	0134+329

TABLE 2  
PARAMETERS OF THE VLA OBSERVATIONS FOR NGC 45

Date of observation .....	1992 June 13
Time on source .....	5 <sup>h</sup>
Field center (1950.0) .....	00 <sup>h</sup> 11 <sup>m</sup> 30.0 <sup>s</sup> −23°27′60.0″
Primary beam at half-power (FWHM) .....	32′
FWHM of synthesised beam .....	42″ × 42″
Total bandwidth .....	1.56 MHz
Central velocity (heliocentric) .....	470 km s <sup>−1</sup>
Central frequency .....	1418.3115 MHz
Number of channels .....	128
Channel separation .....	12.2 kHz
Velocity Resolution .....	2.5 km s <sup>−1</sup>
RMS noise in channel maps .....	1.6 mJy/beam
Conversion factor, equivalent 1 mJy/beam area (low resolution) 42″ × 42″ .....	0.34 K
Maps gridding .....	10″ × 10″ natural weighting no taper
Flux calibrator .....	0134+329



Table 3: *I*-band luminosity profile of NGC 24

Radius (arcsec)	$\mu_I$ (mag arcsec <sup>-2</sup> )	Radius (arcsec)	$\mu_I$ (mag arcsec <sup>-2</sup> )
1.96	18.54	23.37	19.42
2.37	18.57	28.27	19.48
2.87	18.59	34.21	19.61
3.48	18.61	41.39	19.87
4.21	18.63	50.09	20.14
5.09	18.64	60.60	20.58
6.15	18.69	73.33	21.11
7.45	18.83	88.73	21.38
9.01	18.99	107.4	21.95
10.90	19.11	129.9	22.41
13.19	19.19	157.2	23.11
15.96	19.26	190.2	24.22
19.31	19.33		

Table 4: *B*-band Luminosity profile of NGC 45  
(Romanishin et al. 1983)

Radius (arcsec)	$\mu_B$ (mag arcsec <sup>-2</sup> )	Radius (arcsec)	$\mu_B$ (mag arcsec <sup>-2</sup> )
2.3	22.17	142.8	24.95
11.7	22.43	156.8	25.06
16.4	22.54	170.9	25.16
21.1	22.66	184.9	25.36
25.8	22.77	199.0	25.64
30.4	22.90	213.0	25.89
35.1	23.08	227.1	25.99
44.5	23.22	241.1	26.38
58.5	23.53	255.1	26.96
72.6	23.79	269.2	27.12
86.6	24.12	283.2	27.70
100.7	24.29	297.3	27.99
114.7	24.49	311.3	28.43
128.8	24.73	325.4	29.02

TABLE 5  
OPTICAL PARAMETERS OF NGC 24

R.A. (2000) <sup>a</sup> .....	00 <sup>h</sup> 09 <sup>m</sup> 56.6 <sup>s</sup>
DEC. (2000) <sup>a</sup> .....	-24°57'43.0''
Type <sup>a</sup> .....	SA(s)c III
Distance (Mpc) <sup>b</sup> .....	6.8
	(1' = 2.0 kpc)
Mean axis ratio <sup>c</sup> (q = b/a) .....	q = 0.26
Inclination <sup>c</sup> (q <sub>0</sub> = 0.15) <sup>d</sup> .....	i = 78°
Mean position angle <sup>c</sup> .....	θ = 225°
Parameters at μ <sub>B</sub> = 25.0 mag arcsec <sup>-2</sup> :	
Major axis diameter .....	D <sub>25</sub> = 5.9'
Minor axis diameter .....	d <sub>25</sub> = 1.6'
Holmberg radius (μ <sub>B</sub> = 26.6 mag arcsec <sup>-2</sup> ) .	R <sub>H0</sub> = 4.0'
Exponential disk parameters:	
Corrected central surface brightness <sup>e</sup>	I(0) <sub>c</sub> = 20.67
	B(0) <sub>c</sub> = 22.12
Scale length (kpc) .....	α <sup>-1</sup> = 1.42
Total apparent B magnitude .....	B <sub>T</sub> = 12.13
Corrected apparent B magnitude .....	B <sub>T</sub> <sup>0,i</sup> = 11.75
Corrected absolute B magnitude .....	M <sub>B</sub> <sup>0,i</sup> = -17.41
Total blue luminosity <sup>f</sup> .....	L <sub>T</sub> (B) = 1.4 × 10 <sup>9</sup> L <sub>⊙</sub>

<sup>a</sup>de Vaucouleurs et al. 1991 (RC3).

<sup>b</sup>Tully 1988.

<sup>c</sup>For 1.5' ≤ R ≤ 3.0'.

<sup>d</sup>cos<sup>2</sup> i =  $\frac{q^2 - q_0^2}{1 - q_0^2}$  following Bottinelli et al 1983.

<sup>e</sup>Line-of-sight integration correction = 2.5 log R<sub>25</sub> = 1.575 (RC3).

<sup>f</sup> With M<sub>B⊙</sub> = +5.43 (Allen 1976).

TABLE 6  
OPTICAL PARAMETERS OF NGC 45

R.A. (2000) <sup>a</sup> .....	00 <sup>h</sup> 14 <sup>m</sup> 03.2 <sup>s</sup>
DEC. (2000) <sup>a</sup> .....	-23°11'01.0''
Type <sup>a</sup> .....	SA(s)dm IV-V
Distance (Mpc) <sup>b</sup> .....	5.9
	(1' = 1.72 kpc)
Mean axis ratio <sup>d</sup> (q = b/a) .....	q = 0.73
Inclination <sup>c</sup> (q <sub>0</sub> = 0.22) <sup>e</sup> .....	i = 55° ± 5°
Position angle <sup>c</sup> .....	θ = 145° ± 5°
Parameters <sup>d</sup> at μ <sub>B</sub> = 25.0 mag arcsec <sup>-2</sup> :	
Major axis diameter .....	D <sub>25</sub> = 5.8'
Minor axis diameter .....	d <sub>25</sub> = 4.2'
Holmberg radius (μ <sub>B</sub> = 26.6 mag arcsec <sup>-2</sup> ) <sup>d</sup>	R <sub>H0</sub> = 4.8'
Exponential disk parameters <sup>d</sup> :	
Corrected central surface brightness	B(0) <sub>c</sub> = 22.51
Scale length (kpc) .....	α <sup>-1</sup> = 2.20
Total apparent B magnitude <sup>d</sup> .....	B <sub>T</sub> = 11.48
Corrected apparent B magnitude .....	B <sub>T</sub> <sup>0,i</sup> = 11.40
Corrected absolute B magnitude .....	M <sub>B</sub> <sup>0,i</sup> = -17.45
Total blue luminosity <sup>f</sup> .....	L <sub>T</sub> (B) = 1.4 × 10 <sup>9</sup> L <sub>⊙</sub>

<sup>a</sup>de Vaucouleurs et al. 1991 (RC3).

<sup>b</sup>Tully 1988.

<sup>c</sup>Puche & Carignan 1988.

<sup>d</sup>Romanishin et al. 1983.

<sup>e</sup>cos<sup>2</sup> i =  $\frac{q^2 - q_0^2}{1 - q_0^2}$  following Bottinelli et al 1983.

<sup>f</sup>With M<sub>B⊙</sub> = +5.43 (Allen 1976).

Table 7: HI Rotation Curve for NGC 24

Radius (arcsec)	$V_{rot}$ ( $\text{km s}^{-1}$ )	Error ( $\text{km s}^{-1}$ )	Radius (arcsec)	$V_{rot}$ ( $\text{km s}^{-1}$ )	Error ( $\text{km s}^{-1}$ )
40	56.6	6.4	200	103.6	2.2
80	82.5	2.7	240	106.2	1.8
120	91.8	0.8	280	109.4	3.5
160	99.2	0.8	320	109.7	2.0

Table 8: HI Rotation Curve and Position Angle of the kinematical major axis for NGC 45

Radius (arcsec)	$V_{rot}$ ( $\text{km s}^{-1}$ )	Error ( $\text{km s}^{-1}$ )	$P.A.$ ( $^{\circ}$ )	Error ( $^{\circ}$ )	Radius (arcsec)	$V_{rot}$ ( $\text{km s}^{-1}$ )	Error ( $\text{km s}^{-1}$ )	$P.A.$ ( $^{\circ}$ )	Error ( $^{\circ}$ )
42	53.2	3.6	144.0	11.0	336	105.9	0.3	139.3	0.2
84	70.1	1.3	148.6	5.9	378	103.4	1.4	136.5	0.1
126	79.1	1.7	148.2	1.0	420	101.0	0.9	132.7	1.6
168	87.4	0.3	147.0	0.3	462	100.9	1.0	129.0	1.5
210	93.4	0.4	147.2	0.7	504	99.9	1.5	126.4	1.3
252	97.7	2.2	145.9	1.3	546	99.8	0.3	124.6	0.7
294	102.3	1.6	143.0	1.0	588	100.0	0.6	124.9	0.4

TABLE 9  
“BEST-FIT” TWO COMPONENT MODEL FOR NGC 24

<i>Luminous disk component:</i>	
$(\mathcal{M}/L_B)_*$	$2.5 \mathcal{M}_\odot/L_\odot$
$\mathcal{M}_{\text{disk}}$	$3.4 \times 10^9 \mathcal{M}_\odot$
$\mathcal{M}_{\text{HI+He}}$	$7.4 \times 10^8 \mathcal{M}_\odot$
<i>Dark halo component:</i>	
$r_c$	5.6 kpc
$\sigma$	$65 \text{ km s}^{-1}$
$\rho_0$	$0.022 \mathcal{M}_\odot \text{ pc}^{-3}$
<i>At <math>R_{HO}</math> (<math>r=7.9 \text{ kpc}</math>):</i>	
$\rho_{\text{halo}}$	$0.004 \mathcal{M}_\odot \text{ pc}^{-3}$
$\mathcal{M}_{\text{dark}}/\mathcal{M}_{\text{lum}}$	4.0
$(\mathcal{M}/L_B)_{\text{dyn}}$	$15.3 \mathcal{M}_\odot/L_\odot$
$\mathcal{M}_{\text{dark+lum}}$	$2.0 \times 10^{10} \mathcal{M}_\odot$
<i>At last measured point (<math>R=10.5 \text{ kpc}</math>):</i>	
$\rho_{\text{halo}}$	$0.0022 \mathcal{M}_\odot \text{ pc}^{-3}$
$\mathcal{M}_{\text{dark}}/\mathcal{M}_{\text{lum}}$	6.0
$(\mathcal{M}/L_B)_{\text{dyn}}$	$21.2 \mathcal{M}_\odot/L_\odot$
$\mathcal{M}_{\text{dark+lum}}$	$2.8 \times 10^{10} \mathcal{M}_\odot$

TABLE 10  
“BEST-FIT” TWO COMPONENT MODEL FOR NGC 45

<i>Luminous disk component:</i>	
$(\mathcal{M}/L_B)_*$	$5.2 \mathcal{M}_\odot/L_\odot$
$\mathcal{M}_{\text{disk}}$	$5.3 \times 10^9 \mathcal{M}_\odot$
$\mathcal{M}_{\text{HI+He}}$	$2.1 \times 10^9 \mathcal{M}_\odot$
<i>Dark halo component:</i>	
$r_c$	6.2 kpc
$\sigma$	$55 \text{ km s}^{-1}$
$\rho_0$	$0.013 \mathcal{M}_\odot \text{ pc}^{-3}$
<i>At <math>R_{HO}</math> (<math>r=8.3 \text{ kpc}</math>):</i>	
$\rho_{\text{halo}}$	$0.003 \mathcal{M}_\odot \text{ pc}^{-3}$
$\mathcal{M}_{\text{dark}}/\mathcal{M}_{\text{lum}}$	1.8
$(\mathcal{M}/L_B)_{\text{dyn}}$	$18.0 \mathcal{M}_\odot/L_\odot$
$\mathcal{M}_{\text{dark+lum}}$	$1.8 \times 10^{10} \mathcal{M}_\odot$
<i>At last measured point (<math>R=16.7 \text{ kpc}</math>):</i>	
$\rho_{\text{halo}}$	$0.0005 \mathcal{M}_\odot \text{ pc}^{-3}$
$\mathcal{M}_{\text{dark}}/\mathcal{M}_{\text{lum}}$	4.0
$(\mathcal{M}/L_B)_{\text{dyn}}$	$36.2 \mathcal{M}_\odot/L_\odot$
$\mathcal{M}_{\text{dark+lum}}$	$3.7 \times 10^{10} \mathcal{M}_\odot$

TABLE 11  
TWO COMPONENT MODEL FOR NGC 45 WITH  $(M/L) = 2.0$

<i>Luminous disk component:</i>	
$(\mathcal{M}/L_B)_*$	$2.0 \mathcal{M}_\odot/L_\odot$
$\mathcal{M}_{\text{disk}}$	$2.0 \times 10^9 \mathcal{M}_\odot$
$\mathcal{M}_{\text{HI+He}}$	$2.1 \times 10^9 \mathcal{M}_\odot$
<i>Dark halo component:</i>	
$r_c$	4.2 kpc
$\sigma$	$58 \text{ km s}^{-1}$
$\rho_0$	$0.032 \mathcal{M}_\odot \text{ pc}^{-3}$
<i>At <math>R_{HO}</math> (<math>r=8.3 \text{ kpc}</math>):</i>	
$\rho_{\text{halo}}$	$0.003 \mathcal{M}_\odot \text{ pc}^{-3}$
$\mathcal{M}_{\text{dark}}/\mathcal{M}_{\text{lum}}$	4.7
$(\mathcal{M}/L_B)_{\text{dyn}}$	$18.8 \mathcal{M}_\odot/L_\odot$
$\mathcal{M}_{\text{dark+lum}}$	$1.9 \times 10^{10} \mathcal{M}_\odot$
<i>At last measured point (<math>R=16.7 \text{ kpc}</math>):</i>	
$\rho_{\text{halo}}$	$0.0005 \mathcal{M}_\odot \text{ pc}^{-3}$
$\mathcal{M}_{\text{dark}}/\mathcal{M}_{\text{lum}}$	7.8
$(\mathcal{M}/L_B)_{\text{dyn}}$	$35.8 \mathcal{M}_\odot/L_\odot$
$\mathcal{M}_{\text{dark+lum}}$	$3.7 \times 10^{10} \mathcal{M}_\odot$